UAV-Based Analysis of Armour Rock Granulometry and Hydraulic Stability

Alisson Villca[1][a], Muhammad Ali Sammuneh[1][b], Poupardin Adrien[1], Jena Jeong[1], Rani El Meouche[1][c] and Georges Chapalain[2]

[1]*Institut de Recherche (IR), ESTP Paris, 94230 Cachan, France*

[2]*Cerema Risques Eau Mer, Margny-Les-Compiègne, 60280, France*

Keywords: Granulometry, UAV, Photogrammetry, Image Processing, Stability, Monitoring.

Abstract: Dikes worldwide play a crucial role in mitigating flooding risks. Often, armour rocks are placed within the wave impact zone to protect the dike from wave loading. To ensure a dike is in optimal condition the assessment of the hydraulic stability of armour rocks is necessary. This study presents a Granulometric analysis technique, which is based on UAV photogrammetry and optical digital granulometry to evaluate the spatial distribution and possible variations in time of armour rocks granulometry and hydraulic stability. This is a new non-invasive technique with which spatial, temporal changes can be studied. Our study area is located in Camargue, south of France. This low-laying region, exposed to multiple storms, is among the most endangered zones by sea level rise. We concluded that monitoring of the dike is possible using this technology the optical granulometric analysis could be performed on UAV images. We conducted granulometry distribution calculations for armour rocks, even when they were covered with moss. Our findings show the spatial variation of granulometry along the dike. In specific areas of interest where hydraulic stability was assessed, based on the granulometry results, we have found areas with low hydraulic stability that need to be investigated more thoroughly.

1 INTRODUCTION

The grading curve analysis along with characteristic sizes of non-cohesive materials is a traditional and important method that can provide important parameters for hydraulic modelling. To obtain such information laboratory and in situ tests exist. Laboratory sieving involves time-consuming and effort-intensive activities just the same in situ techniques, which uses a grid system to measure single pebbles (Wolman, 1954) or uses instead a sampling line (Fehr, 1987), can be just as time consuming.

To overcome these limitations tools for automatic optical granulometry were developed. These non-intrusive, low cost methods can obtain grain size distributions for non-cohesive materials (Graham et al., s. d.) (Detert & Weitbrecht, 2012) (Buscombe, s. d.). For the granulometric, analysis of riverbed depositions a matlab-based tool was developed, BASEGRAIN, that can recognize, classify and analyse grain images (Detert & Weitbrecht, 2012).

Basegrain analysis results can still be meaningful despite being used with photos taken in suboptimal conditions. (Detert & Weitbrecht, s. d.)

The potential of the combination of Unmanned Aerial Systems (UAS) technology and optical granulometry was studied in previous works. A peak discharge estimation in the town of Mandra, Greece (Andreadakis et al., 2020). The median particle size derived from the granulometric curves were used to estimate run-off. They compared the results of run-off estimations calculated with data from UAV and GNSS surveys which showed minimal difference. (Lagogiannis & Dimitriou, 2021) combined UAV-sensed data with empirical hydraulic equations to produce accurate discharge estimations in 10 out of 17 sites. The estimation of the manning coefficient was based on percentile of particles (d_{90}, d_{84} and d_{50})

[a] https://orcid.org/0009-0005-8274-9940
[b] https://orcid.org/0009-0008-4977-7386
[c] https://orcid.org/0000-0001-5063-6638

Villca, A., Sammuneh, M., Adrien, P., Jeong, J., El Meouche, R. and Chapalain, G.
UAV-Based Analysis of Armour Rock Granulometry and Hydraulic Stability.
DOI: 10.5220/0012703700003696

In *Proceedings of the 10th International Conference on Geographical Information Systems Theory, Applications and Management (GISTAM 2024)*, pages 62-70
ISBN: 978-989-758-694-1; ISSN: 2184-500X

derived from optical granulometric curves. Optical granulometry was applied to riverbeds in Japan, the accuracy of the optical method was compared to field measurements showing great coincidence except for the finer grains where the resolution of the image plays a key role (Kadota et al., s. d.).

The aim of this study is to combine these two technologies: UAV photogrammetry and digital optical granulometry to carry out the monitoring of an earthen dike's armour rocks and establish the procedure for the treatment of UAV imagery to execute the granulometry analysis and ultimately evaluate the hydraulic stability of the armour rock layers. In section 2 we will see the study-site. Section 3 is divided into three main sections UAV photogrammetry, optical granulometry and hydraulic stability analysis. In section 4 the results are discussed and finally in section 5 conclusions are drawn.

2 CASE STUDY

Located in the south of France, Camargue is a low-lying region, exposed to multiple storms, see figure 1. It is among the most endangered zones by rise in sea level (Pörtner & Roberts, s. d.).

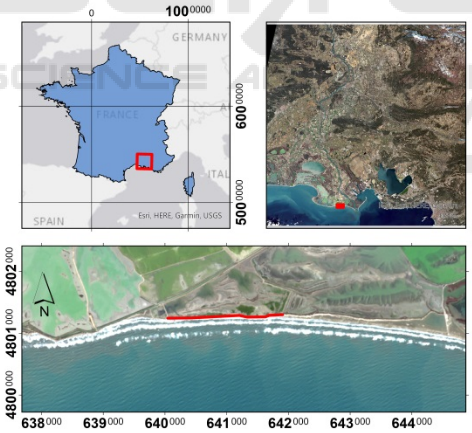

Figure 1: Location of study area in south of France. In the top-left view France is highlighted. The red area represents sentinel 2 tile 31TFJ projected on the UTM – zone 31N (Universal Transverse Mercator). The top-right view shows the tiled sentinel-2 image (date: 28 February 2023) and the red box highlights the zoomed area of the bottom view. The dike "Quenin" length is shown in red.

The two-kilometer long earthen dike is located to the west of the Pharaman lighthouse. During storm surges it has to protect the salt marshes from inundation.

3 MATERIALS AND METHODS

3.1 UAV Photogrammetry

3.1.1 Drone Specifications

In this study a DJI Phantom 4 Advanced was deployed with a 1-inch 20-megapixel CMOS sensor. The maximum flight time being 30 minutes limited the survey area, thus the total area was divided into three survey zones. The mission took place on 12 April. Table 1 summarizes the principal characteristic of the sensor.

Table 1: Sensor specifications.

Sensor	1" CMOS, Pixels: 20M, Size: 12.83mmx8.55mm
Lens	FOV 84° 8.8 mm/24 mm
Image size	3:2 Aspect Ratio: 5472 × 3648
Filetype	JPEG

Ground sampling distance (GSD) can be approximated by the following formula:

$$\text{GSD} = \frac{S_w}{IM_w} \times \frac{H}{f} \tag{1}$$

Where S_w and IM_w is the sensor and image width respectively. The aircraft height is H and f is the camera focal length. In our case, GSD is approximately 31.1mm for a 120m flight height. The selected GSD should allow detection of the armour rocks with mean D_{50} values from 250 to 850mm. Following a rule of thumb so that every grain is represented by a minimum number of pixels b>10px (Detert & Weitbrecht, 2012) we note that the for the lower D_{50} value the number of pixels is lower than 10px, but for the larger diameter the condition is met.

3.1.2 Flight Planification

During the data acquisition phase, Figure 2 two drone surveys were done for the April mission. The first survey took nadir images at 70% overlap along the dike (149). The second mission took nadir images with 30% overlap in an area 900m from the coast to estimate shallow bathymetry (238).

It is necessary to verify in situ if the required overlap is achieved. The wind may affect the drone speed and reduce the number of overlapped images in certain zones. To overcome this inconvenience a combination of the images from both missions was used. From the overlap map, it can be seen that an offset distance from the flight area and study area must be foreseen to ensure more than five overlapped images in the study area.

3.1.3 Ground Control Points

Ground Control Points (GCP's) and Checkpoints (CP's) were marked with a red spray following a zigzag pattern on the dike crest see figure 3 coordinate measurement were made on the same day with a GNSS multiband antenna IP 67 and a ZED-F9P RTK receiver, in total 13 points were measured.

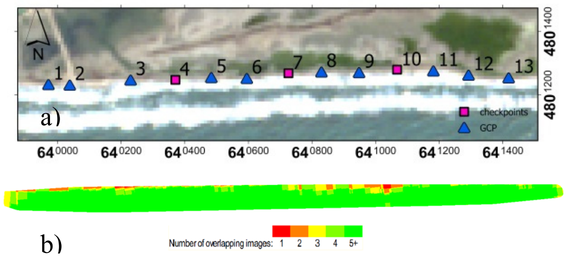

Figure 2: a) GCP's and CP's distribution along the dike, b) Combined missions overlap map.

The centipede GNSS network, an open source collaborative network of more than 300 homemade RTK bases across France, was used. It allowed us to benefit from RTK centimetre positioning for free (*Le Reseau Centipede RTK*, s. d.). The smartphone SW maps application was used to collect, store and visualize the coordinates (*SW Maps - Mobile GIS*, s. d.). The consistency and reliability of this equipment, software and network has been validated in previous studies. (Sammuneh et al., 2023)

Figure 3: GCP's following a zigzag pattern on the crest of the dike.

3.1.4 Photogrammetric Processing

The data processing is done using Pix4D (version 4.5.6), were all GCP's and CP's targets were manually marked at their centers to ensure accurate geo-referencing. For accuracy assessment, Root Mean Square Error (RMSE) is used, see table 2, for a combination of both surveys with 178 images with 70% and 30% overlap. Previous studies have evaluated the level of accuracy that can be achieved with UAV equipment (El Meouche et al., 2016) (Jiménez-Jiménez & Ojeda-Bustamante, 2021). Just the same vertical error in our case (Z) is significantly larger than planar error (X, Y).

Table 2: Results of the photogrammetric block adjustment. Survey April 2023.

RMSE	X(m)	Y(m)	Z(m)
GCP's	0.005	0.011	0.017
CP's	0.070	0.030	0.347

The workflow diagram in figure 4 shows the different steps from data acquisition, data processing and data analysis. The pix4D software proposes a photogrammetric technique based on structure from motion algorithm based on three stages. First, the position of the images is extracted from the EXIF metadata and specific features called key-points are found on every image in order to find matching points in overlapped images. This makes it possible to know the camera position and orientation to carry out an internal and external camera calibration during the bundle block adjustment. Then automatic tie points are detected in the image to compute its 3D position and point cloud densification allows more tie points to be created. Finally, the products obtained include the digital surface models, ortho-image and reflectance maps.

Rematch and optimize was used to compute more matching points between images and therefore more automatic tie points through re-optimization of internal and external camera parameters. The internal camera parameters from the EXIF metadata are focal length, two principal point offsets (x, y), three radial (R_1, R_2, R_3) and two tangential (T_1, T_2) distortion coefficients. The external camera parameters are defined by the position of the camera projection center (T_x, T_y, T_z) and the rotation matrix defined by the camera orientation ($R_x(\omega), R_y(\phi), R_z(\kappa)$). (*Professional Photogrammetry and Drone Mapping Software*, s. d.)

3.2 Digital Optical Granulometry

Digital optical granulometry is a non-invasive technique based on the analysis of digital images after a scaling factor is applied. In this study the Basegrain software is used to carry out the granulometry analysis (Detert & Weitbrecht, 2012).

Areas of interests were chosen along the dike's longitudinal axis every 100m approximately. At the same time 3 zones of interest were defined along the transversal axis of the dike, see figure 5. Zone A is the area in the inner slope with small granular

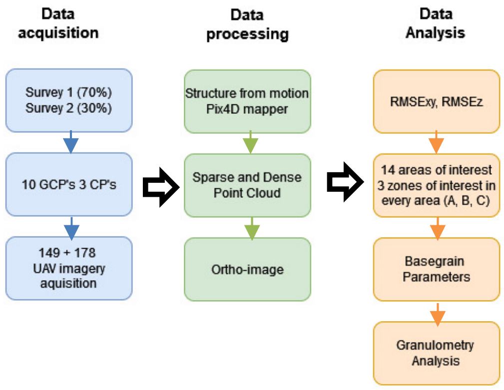

Figure 4: Workflow of photogrammetric and optical granulometry analysis processing.

material compared to the armour rocks. Zone B is the outer slope closest to the crest-dike. Finally, the C zone has armour rocks, covered with moss, in the wave impact area.

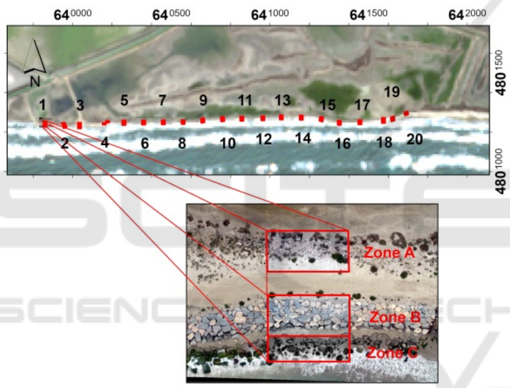

Figure 5: 20 Areas of interest along the dike and three zones of interest, zone A (inner slope), zone B (outer slope near the crest), zone C (outer slope near the wave impact zone). Universal Transverse Mercator, Zone 31N coordinates.

3.2.1 Basegrain Software

Basegrain has multiple steps to obtain the granulometric curves, see figure 6, first a procedure to detect the interstices between grains by double grayscale threshold (1), to determine further interstices a morphological bottom hat transform is applied (2). Then the canny and sobel method is used to find grain edges (3) then the separation of single grains is made by watershed transform (4). Next, grain areas are measured and replaced with ellipsis of the same normalized second central moments (5). Finally, the analysis of results follows the Fehr's approach. (Detert & Weitbrecht, 2012)

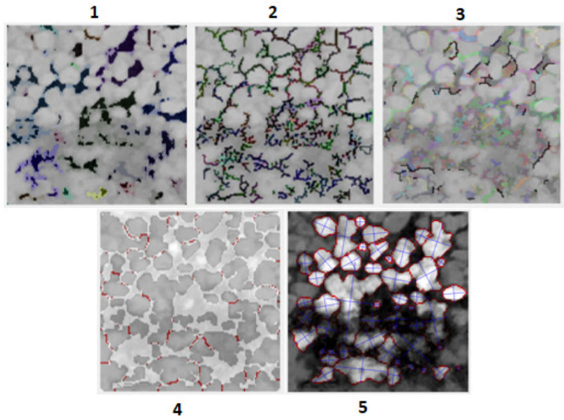

Figure 6: The result of the different Basegrain steps (1 to 5) for zone of interest A9.

3.2.2 Basegrain Parameters

In this study for zones A and B the default parameters were sufficient to detect a great majority of the armour rocks, however for zones C some changes had to be made as these armour rocks were covered with moss and the automatic detection with default parameters worked poorly as seen in figure 7. This is because in locations with partly wetted stones the detection algorithm separates the armour rocks in various parts.

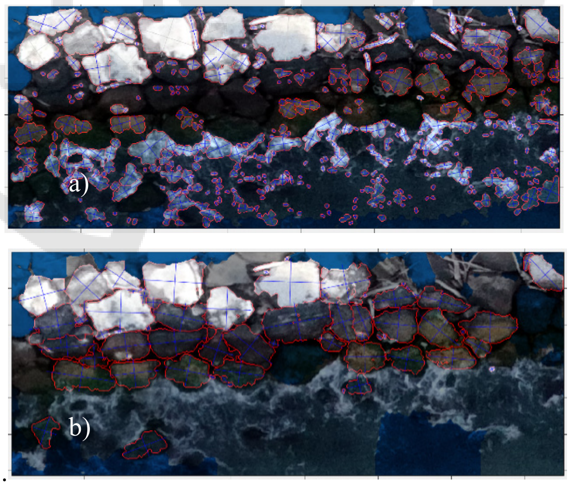

Figure 7: Automatic armour rock size automatic detection after steps 1 to 5 for zone C9, a) Automatic grain detection with default parameters, b) with modified parameters.

The modified parameters include for step (1) the ***blocSizG*** *(block size gray threshold)* and the ***facgraythr1*** *(factor gray threshold 1).* The first is the size of the block in which Otsu's thresh value is determined and was modified from 32 to 4. The second is the multiplier that determines definite interstices; it was changed from 0.8 to 0.5. For step (2) the ***puxCutoff*** (*bottom-hat interstices)* was modified from 1 to 8. At least 5 minutes manual splitting, merging or removal was necessary for all images.

Once the granulometry curves have been obtained the median sieve size D_{50}, can be calculated for every area of interest in zone C. The median sieve size D_{50} and the median nominal diameter D_{n50} are proportional, $D_n = 0.84D$ experimentally determined for different rock types and grading. The median mass M_{50} and median size sieve D_{50} are related using the conversion factor F_S = 0.60 (Rock Manual 2007)

$$M_{50} = \rho \ \times 0.6\, {D_{50}}^3 \tag{2}$$

3.3 Stability Criteria for Armour Units

After various model tests with two-diameter thick layer of armour rocks a formula was developed by (Van der Meer 1998) to assess the stability of rock protection under wave attack. Because $\xi_m < \xi_{mc}$ we will use the formulae for plunging waves (5)

$$\xi_{mc} = \left(6.2 P^{0.31} \sqrt{\tan \propto}\right)^{\frac{1}{P+0.5}} \tag{3}$$

$$\xi_m = tan\alpha / (\frac{2\pi H_S}{g T_m^2}))^{0.5}. \tag{4}$$

$$\frac{H_S}{\Delta D_{n50}} = 6.2\, P^{0.18} \left(\frac{S_d}{\sqrt{N_w}}\right)^{0.2} \xi_m^{-0.5} \tag{5}$$

For the breaker parameter ξ_m, α is the dike slope angle, T_m is the mean period and g is the gravitational constant. WhereH_S, is the significant wave height at the toe of the structure, $\Delta = \rho_r / \rho_w - 1$ is the dimensionless relative buoyant density of the armour rocks. Where ρ_r and ρ_w are the densities of rock and seawater Δ is around 1.58 for granite in seawater.

P, is the notional permeability factor, S_d the damage level, N_w the wave number and ξ_m called the breaker parameter. P represents the influence of the permeability of the structure on the stability of the armour layer, in this case we will assume P = 0.5. This means the armour rock layer has a thickness of at least $2D_{n50}$ on top of the core material (see figure 8). The number of waves N_w depends on the storm duration, in our case 6 hours.

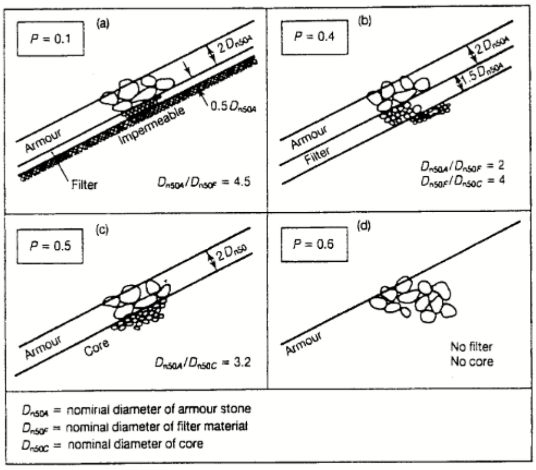

Figure 8: Notional permeability factor for various structures. (Van Der Meer, 1988).

The damage level $S_d$depends on the slope angle (see figure 9) of the structure and takes into account settlement and displacement a physical description would be the number of cubic stones with side D_{n50} eroded within a D_{n50} −wide strip of the structure. (Van Der Meer, 1988). The slope angle in our case is between 20° and 50°, a slope of 1:1.5 is the closest value corresponding to a 34° slope angle.

slope	initial damage	intermediate damage	failure (under layer visible)
1:1.5	2	3-5	8
1:2	2	4-6	8
1:3	2	6-9	12
1:4	3	8-12	17
1:6	3	8-12	17

Figure 9: Limits of Sd for a two-diameter thick armour layer. (Van Der Meer, 1988).

For the local significant wave height at toe of the structure H_s we will use the results of a previous study where one dimensional waves were propagated from deep water taking into account the actual bathymetry with Tomawac. A set of simulations were run with varying boundary significant wave height H_{m0} = 3m, 5m, and 8m, initial mean water level η = 0.2m, 0.4m, 0.5m, 0.8m, 1.1m, 1.5m and frequencies f = 0.187 Hz, 0.147 Hz, 0.117 Hz. (Paul et al., 2020)

4 RESULTS AND DISCUSSION

4.1 Granulometry Results

The final graph analysis chosen to represent the results were the quasi-sieve throughput (qi[-]), based on the top view b axis by number on a logarithmic scale. The Basegrain derived grain distribution for the different zones of interest are shown in figures 10, 11 and 12. For zone A, the inner slope area, the regularity of the grain size distribution is evident along the dike.

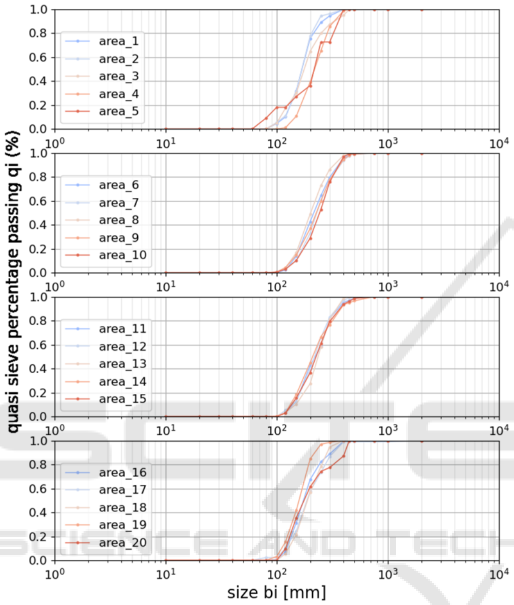

Figure 10: Granulometric curves for zone A, located in the inner slope of the dike.

For zone B, the outer slope zone near the crest, there is a strong dominance of coarser material, at the end and the beginning however, the finer grains percentage increases. Finally, for zone C, the outer slope near the wave impact area, there is dominance of coarser material along the dike except for some areas in the middle 1, 2, 4, 7, 8, 11 and 13.

For zone C, granulometry is very heterogeneous already some areas of interest stand out at the beginning and end of the dike, areas of interest number 4, 7, 11 and 13 are notable for its low median diameter value D_{50} and percentiles values in general. The areas of interest stop at 18 because in this location the wave impact area has no armour rocks but sand.

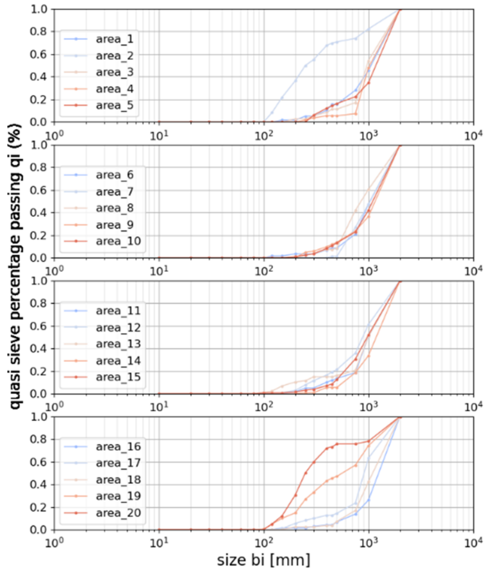

Figure 11: Granulometric curves for zone B, located in the outer slope of the dike near the crest.

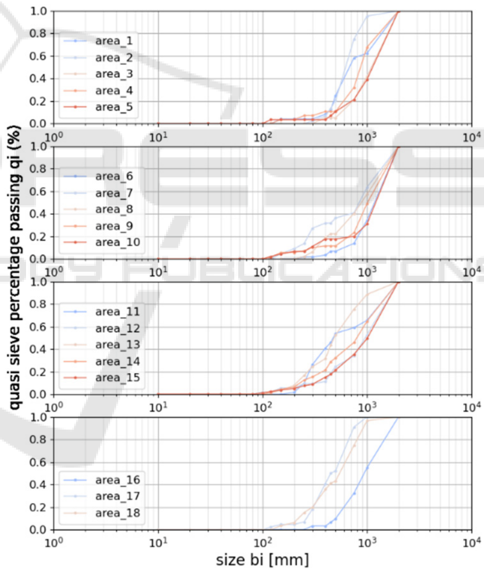

Figure 12: Granulometric curves for zone C, located in the outer slope of the dike near the wave impact area.

In figure 13 the estimated diameters of the coarse fraction grain percentiles D_{10}, D_{15}, D_{20}, D_{50}, D_{65}, D_{70}, D_{80}, D_{85}, and D_{97} and indicate the armour rock size for a particular percent finer value. For zone A, the homogeneity of detected granulometry is again confirmed while for zone B this homogeneity is present only in the central part of the dike both the beginning and end show much greater quantities of fine material.

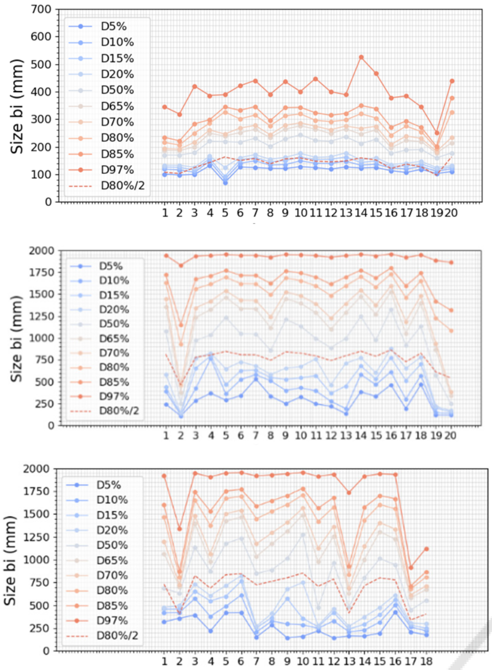

Figure 13: Grain size percentiles values D_{10}, D_{15}, D_{20}, D_{50}, D_{65}, D_{70}, D_{80}, D_{85}, and D_{97}, estimated using Basegrain for zones A, B and C versus the areas of interest in the x axis.

A limitation of optical granulometry technique in our case for zone A is that spatial resolution is not sufficient to represent every grain main axis b with at least 10 pixels. For zones B and C this condition is met. Another limitation is that wetted or moss-covered rocks will require the tuning of Basegrain parameters as we did and some manual editing. However, a huge advantage is that both spatial and temporal monitoring of granulometry can be done with relatively low cost and time.

4.2 Hydraulic Stability Results

To study the stability of the armour rock layer in zone C the significant wave height for the following areas is available 4, 5, 6, 7, 8, 10, 11, 12, 13 and 14 from a previous study. The hydraulic stability results are shown in figure 14.

The significant wave heights at the toe of the dike H_s depend on the boundary wave height H_{m0} initial mean water level η and position along the dike (areas). From figure 14a) where $H_{m0} = 3m, T = 5.34s$ damage levels for all areas are below initial damage limit except for areas 11 and 13 for all initial still water levels $\eta = 0.2 - 0.8m$. Let's remember that areas 4, 7, 11 and 13 have low median diameter values. As boundary wave heights increases in figure 14b) $H_{m0} = 5m, T = 6.80s$ other areas such as 4, 7, 8 and 14 now surpass the initial damage limit value ($S_d < 2$) for initial still water levels $\eta = 0.8 - 1.1m$. But only areas 11, 13 and 14 go beyond failure damage level ($S_d > 8$).

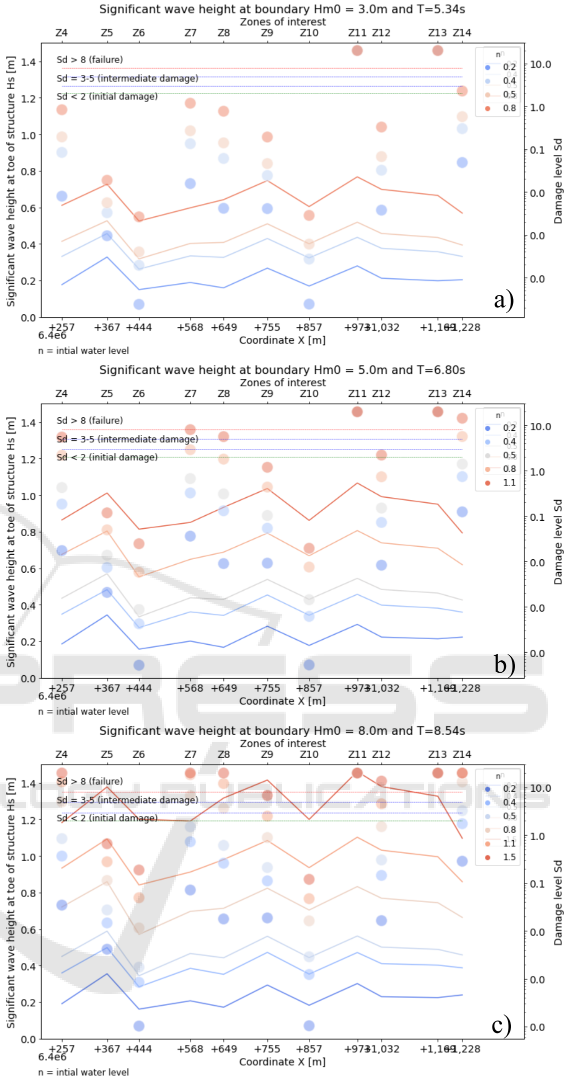

Figure 14: Significant wave height at toe of the dike H_s (left vertical axis), damage levels S_d along the dike (right vertical axis), for areas of interest 4, 5, 6, 7, 8, 9, 10, 11, 12, 13 and 14 (upper horizontal axis) for varying initial still water levels η (see legend). The coordinate of the area of study (UTM Zone 31N) are in the lower horizontal axis.

Finally in figure 14c) where significant wave height at boundary increases to $H_{m0} = 8m, T = 8.54s$ the areas going beyond failure damage level are adding up 4, 7, 8 and 12 for high initial still water levels between $\eta = 0.8 - 1.1m$. The areas remaining under initial damage level under all circumstances are 5, 6 and 10. Notably area 14 reaches intermediate damage levels for low $\eta = 0.4 - 0.5m$ values. Damage levels exceeding failure levels reaching 15-20 values mean an S shaped profile is developing this is the case of areas 11 and 13 for $H_{m0} = 3 - 5m$. The number of areas increases to 6 (areas 4, 7, 8, 11, 13 and 14) when $H_{m0} = 8m$.

5 CONCLUSIONS AND WAY FORWARD

This study presents a non-invasive technique of granulometric analysis based on UAV-based photogrammetry and optical digital granulometry in order to evaluate the stability of its armour rock layer on the wave impact zone. This technique is tested on an earthen dike located in the south of France were monitoring of an earthen dike exposed to storms is necessary.

Measurements were obtained in April 2023, the images were processed in pix4D to obtain a georeferenced ortho-image then the Basegrain tool is used to analyse armour rock size properties in 20 areas of interest along the dike, for three zones of interest A (inner slope), B (outer slope near the crest) and C (outer slope in the wave impact zone). The adjustment of some software parameters allowed automated detection of armour rocks covered with moss.

Once the grain size distribution is obtained the spatial variation along the dike was evaluated. The median sieve size by a conversion factor let us approximate the median nominal diameter to evaluate the stability of the armour rock layer for different sea-states.

The short time application and flexibility of the UAV and optical granulometry, in comparison with traditional methods, makes this approach an effective tool for approximation of granulometry and stability of armour rocks. The ability of multiple data collection offers the potential of spatial and temporal monitoring of the dike.

Several assumptions were made to apply the van der Meer formulas, parameters like, notional permeability factor, Number of waves, storm duration, and dike slope. Looking ahead, this study aims examining the variability of the different parameters assumed to be constant along the dike.

REFERENCES

Andreadakis, E., Diakakis, M., Vassilakis, E., Deligiannakis, G., Antoniadis, A., Andriopoulos, P., Spyrou, N. I., & Nikolopoulos, E. I. (2020). *Unmanned Aerial Systems-Aided Post-Flood Peak Discharge Estimation in Ephemeral Streams*.

Buscombe, D. (s. d.). *SediNet : A configurable deep learning model for mixed qualitative and quantitative optical granulometry*.

Detert, M., & Weitbrecht, V. (s. d.). *Determining image-based grain size distribution with suboptimal conditioned photos*.

Detert, M., & Weitbrecht, V. (2012). *Automatic object detection to analyze the geometry of gravel grains – a free stand-alone tool*.

Fehr, R. (1987). Einfache Bestimmung der Korngrössenverteilung von Geschiebematerial mit Hilfe der Linienzahlanalyse. *Schweizer Ingenieur und Architekt*, *105*(38), 1104-1109. https://doi.org/10.5169/seals-76710

Graham, D. J., Rice, S. P., & Reid, I. (s. d.). *A transferable method for the automated grain sizing of river gravels*.

Jiménez-Jiménez, S. I., & Ojeda-Bustamante, W. (2021). *Digital Terrain Models Generated with Low-Cost UAV Photogrammetry : Methodology and Accuracy*.

Kadota, A., Asayama, C., & Ndwambi, I. D. (s. d.). *Image analysis of grain size distribution around area of sand deposition*.

Lagogiannis, S., & Dimitriou, E. (2021). *Discharge Estimation with the Use of Unmanned Aerial Vehicles (UAVs) and Hydraulic Methods in Shallow Rivers*.

Le Reseau Centipede RTK. (s. d.). Centipede RTK. Consulté 17 mai 2023, à l'adresse https://docs.centipede.fr/

El Meouche, R. E., Hijazi, I., Poncet, P., Abunemeh, M., & Rezoug, M. (2016). *UAV PHOTOGRAMMETRY IMPLEMENTATION TO ENHANCE LAND SURVEYING, COMPARISONS AND POSSIBILITIES.*

Paul, T., Lutringer, C., Poupardin, A., Bennabi, A., Jeong, J., & Sergent, P. (2020). *Wave overtopping and overflow hazards : Application on the Camargue sea-dike*.

Pörtner, H.-O., & Roberts, D. C. (s. d.). *Climate Change 2022 : Impacts, Adaptation and Vulnerability*.

Professional photogrammetry and drone mapping software. (s. d.). Pix4D. Consulté 17 mai 2023, à l'adresse https://www.pix4d.com/

Sammuneh, M. A., El Meouche, R., Eslahi, M., & Farazdaghi, E. (2023). Low-Cost Global Navigation Satellite System (Low-Cost GNSS) for Mobile Geographic Information System (GIS). In M. Ben Ahmed, A. A. Boudhir, D. Santos, R. Dionisio, & N. Benaya (Éds.), *Innovations in Smart Cities Applications Volume 6* (p. 105-117). Springer International Publishing. https://doi.org/10.1007/978-3-031-26852-6_10

SW Maps—Mobile GIS. (s. d.). Consulté 1 février 2024, à l'adresse http://swmaps.softwel.com.np/

Van Der Meer, J. W. (1988). Deterministic and Probabilistic Design of Breakwater Armor Layers. *Journal of Waterway, Port, Coastal, and Ocean Engineering*, *114*(1), 66-80. https://doi.org/10.1061/(ASCE)0733-950X(1988)114:1(66)

Wolman, M. G. (1954). A method of sampling coarse river-bed material. *Eos, Transactions American Geophysical Union*, *35*(6), 951-956. https://doi.org/10.1029/TR035i006p00951